Weather and Climate Extremes 37 (2022) 100463

Contents lists available at ScienceDirect

Weather and Climate Extremes

journal homepage: www.elsevier.com/locate/wace

Towards observation- and atmospheric model-based early warning systems for meteotsunami mitigation: A case study of Korea

Myung-Seok Kim [a], Seung-Buhm Woo [a,*], Hyunmin Eom [b], Sung Hyup You [c], Hye Min Lee [a]

[a] Department of Ocean Sciences, Inha University, Incheon, 22212, Republic of Korea
[b] Marine Meteorology Division, Korea Meteorological Administration, Seoul, 07062, Republic of Korea
[c] Earthquake and Volcano Policy Division, Korea Meteorological Administration, Seoul, 07062, Republic of Korea

ARTICLE INFO

Keywords:
Korean Peninsula
Meteotsunami
Air pressure disturbance
Early warning system
Observation-based monitoring system
Lead time problem
Atmospheric model

ABSTRACT

A traveling air pressure disturbance of several hPa over a short period (5–10 min) can generate tsunami-like waves in coastal areas owing to a multi-resonant mechanism. In recent years, pressure-forced meteotsunamis have been regularly reported over the Korean Peninsula. However, the Korean meteotsunami early warning system does not always provide sufficient lead time. The early warning system comprises two-segmented zones for tracking the intensity and propagation of air pressure disturbances via 89 meteorological stations in the precaution (offshore islands) and warning zones (coastline and inland areas). To address the lead time problem in the current observation-based monitoring system, we used an atmospheric model with a horizontal resolution of 1.5 km, the Korea Meteorological Administration's local data assimilation and prediction system (LDAPS). The ability of the LDAPS to detect air pressure disturbances was tested for a widespread and destructive meteotsunami event that occurred on March 4, 2018. The detection capability of significant air pressure disturbances (>1.5 hPa/10 min) was 67% in the precaution zone, and the propagation pattern (direction, speed, and spatial scale) was reasonably consistent with the monitoring results. Based on LDAPS prediction and the established observation-based monitoring system, monitoring operators can determine the potential meteotsunami risk from the open Yellow Sea beyond the observation system with sufficient lead time. This case study contributes to developing observation- and atmospheric model-based early warning systems for meteotsunami mitigation. An early warning of tsunamigenic disturbances in the Korean Peninsula is expected to be provided with the LDAPS-based modeling system using a high-resolution atmosphere-ocean coupled model shortly.

1. Introduction

In recent decades, interest in unexpected floods in marine and coastal areas has increased due to sea level rise caused by global warming (Ferrarin et al., 2021). Meteotsunamis are a natural hazard generated by multiple resonances (Monserrat et al., 2006), propagate and amplify owing to air pressure disturbances (i.e., rapid changes in air pressure during a short period). This phenomenon is characterized by widespread and hidden flash floods in coastal areas (Liu and Wu, 2022). Interestingly, tsunami-like waves with an atmospheric origin traveling over a distance of thousands of kilometers have been reported in the Balearic Islands, Mediterranean and Black seas, North-East Atlantic, North and South America, East Asia, and the Persian Gulf: specifically at mid-latitudes of the Northern and Southern Hemispheres (Vilibić et al., 2021).

Meteorological and non-seismic tsunamis, which are much lower in intensity than seismic tsunamis but occur more frequently, have the same period bands ranging from 2 min to 2 h as the seismic tsunamis (Pattiaratchi and Wijeratne, 2015). Unlike typhoons and storm surges, meteotsunamis can be triggered even by small-scale atmospheric disturbances and occur under bad and good weather conditions (Rabinovich, 2020). In particular, the magnitude of the simulated meteotsunamis is significantly sensitive to the small-scale characteristics of atmospheric disturbances owing to slight differences in initial conditions or model parameters (Denamiel et al., 2019; Mourre et al., 2021). These characteristics make it challenging to predict meteotsunamis accurately. Attempts are being made worldwide to develop an early warning system to prevent meteotsunami disasters based on the resonance process, which is at the heart of the meteotsunami generation. Destructive meteotsunamis are the combined effects of the Proudman

* Corresponding author.
E-mail address: sbwoo@inha.ac.kr (S.-B. Woo).

https://doi.org/10.1016/j.wace.2022.100463
Received 26 December 2021; Received in revised form 17 March 2022; Accepted 3 May 2022
Available online 6 May 2022
2212-0947/© 2022 The Authors. Published by Elsevier B.V. This is an open access article under the CC BY-NC-ND license (http://creativecommons.org/licenses/by-nc-nd/4.0/).

resonance due to the coupled propagation of air pressure disturbances and long waves in the open sea and chain amplification that occurs for the pre-amplified long waves directed toward the continental shelf and harbor (Rabinovich, 2009). Accordingly, substantial efforts have been made to monitor the characteristics of air pressure disturbances (e.g., intensity, speed, and direction) that are favorable for meteotsunami generation before entering enclosed basins.

Many studies have suggested observation- and model-based monitoring systems for early warning of meteotsunami occurrence. As the oldest observation-based monitoring approach, traveling air pressure disturbances have been monitored in real-time using multiple meteorological stations situated on offshore islands (Jansà and Ramis, 2021; Vilibić et al., 2016). The spatiotemporal distribution of the weather radar reflectivity was also tracked because it is a proxy variable for air pressure disturbances (Wertman et al., 2014). Deep-ocean assessment and reporting of tsunami (DART) buoys and moored surface buoys have been utilized in open-ocean areas beyond meteorological networks and weather radar coverage (Angove et al., 2021; Titov and Moore, 2021). As a new approach to early detection, anomalous surface current patterns were identified at a fine spatiotemporal scale using coastal high-frequency radar (oceanographic radar) systems (Domps et al., 2021). Meanwhile, potential meteotsunami development was studied on the synoptic scale by assessing tsunamigenic synoptic conditions from the ERA-Interim atmospheric reanalysis dataset (Šepić et al., 2016; Vilibić et al., 2018). In recent model-based monitoring systems, a high-resolution atmospheric model with a horizontal resolution ranging from 1.5 to 6 km was used to capture the air pressure disturbances that rapidly change in the time domain and move in space (Denamiel et al., 2019; Shi et al., 2019). To improve the realism of meteotsunami predictions, different parameterization schemes have been adapted to the high-resolution atmospheric model as an ensemble approach (Mourre et al., 2021). Furthermore, coupled or offline simulations (atmosphere-ocean) have been attempted to forecast and warn against coastal flooding characterized by the multi-resonant mechanism, as mentioned above (Huang et al., 2021; Romero et al., 2019; Tojčić et al., 2021).

In the Korean Peninsula, meteotsunami-induced unexpected coastal flooding causes human and property damage every year between March and June, from spring to early summer (Choi et al., 2014; Ha et al., 2018; Kwon et al., 2021). Historical meteotsunami events in the Korean Peninsula are characterized by frequent and local amplification in multiple harbors, especially vulnerable to specific resonant periods of less than 30 min (Kim et al., 2021b). Thus, the Korea Meteorological Administration (KMA) uses 89 automatic weather stations (AWSs) and weather radar systems to monitor atmospheric conditions favorable for pressure-forced meteotsunami generation (i.e., intensity and propagation of air pressure disturbance) before atmospherically induced ocean waves propagate to the harbor entrance (Kim et al., 2021a). To assess the established early warning system, a test operation for real-time monitoring was performed for two months (March to April) in 2018. As a result, the meteotsunami event on March 4, 2018, was classified as a widespread and destructive meteotsunami event considering a 50% occurrence rate (ratio between the number of tide gauges where the meteotsunami occurred and the total number of tide gauges available) and a combined threshold criterion based on a four-sigma value with a minimum wave height greater than 20 cm (Kim et al., 2021b). Fortunately, no cases of meteotsunami damage have been reported in the Korean Peninsula since the operation of the early warning system. However, according to a recent progress report, the lead time of meteotsunami warnings is insufficient for the worst-case scenario (Kim et al., 2022). The KMA installed and tested moored surface buoys (meteorological and oceanographic networks) in the open Yellow Sea, approximately 200–300 km away from the 89 AWSs on the Korean Peninsula, to provide sufficient lead time. However, sudden air pressure disturbances fluctuating for a short period cannot be detected as buoy data are sampled at 30 min intervals because of satellite communication and battery power limitations in the open sea.

Under these circumstances, an early warning system based on an atmospheric model is necessary to overcome the lead time issue of the established observation-based monitoring system. This study assessed the performance of the local data assimilation and prediction system (LDAPS), a high-resolution atmospheric model operated by KMA. The predictability of air pressure disturbances during the meteotsunami event on March 4, 2018, was evaluated by applying the monitoring protocol used in the current warning system to the LDAPS. In summary, our study had three main objectives: (i) to assess the performance of the LDAPS for determining air pressure disturbances (propagation pattern, magnitude, and arrival time), (ii) to propose how the LDAPS can be utilized in the established warning system, and (iii) to measure the predictability of LDAPS-based meteotsunami modeling in the future.

2. Meteotsunami warning system

2.1. Air pressure disturbance and jump

Widespread and destructive air pressure disturbances and meteotsunamis propagating over almost 3,000 km have been reported in the Mediterranean and Black Sea region (Šepić et al., 2015b). The intensity and propagation patterns of sudden air pressure disturbances (direction, speed, and spatial scale) are important elements that influence the occurrence and propagation of meteotsunamis (Denamiel et al., 2020). Consequently, the KMA has begun monitoring air pressure disturbances using the AWS network over the Korean Peninsula (Kim et al., 2021a). Air pressure disturbance refers to the rate of pressure change over a specific time window (Šepić and Vilibić, 2011; Šepić et al., 2009). In the monitoring system, the air pressure disturbance was calculated as follows:

$$\Delta PD^{t}{}_{i} = \left| P^{t}{}_{i} - P^{t-10}{}_{i} \right| \quad (1)$$

where $\Delta PD^{t}{}_{i}$ is the rate of pressure change over 10 min, $P^{t}{}_{i}$ and $P^{t-10}{}_{i}$ are the air pressures at the AWS or model grid i at time t and t minus 10 min (0, 10, 20, 30, 40, and 50 min). The operating time of the monitoring system (10 min) was determined by considering the file transfer protocol (FTP) download response time from each AWS to the KMA. The level of air pressure disturbance favorable for meteotsunami generation was calculated to be 1.5 hPa/10 min based on data obtained from the test operation and monitoring reports of destructive meteotsunami events over the Korean Peninsula. An air pressure disturbance above the corresponding intensity is classified as an air pressure jump.

2.2. Pressure-forced meteotsunami event on March 4, 2018

On March 4, 2018, strong and widespread air pressure jumps propagated over the Korean Peninsula with an average intensity of 2.6 hPa/10 min at 32 AWSs of the 89 AWSs (Kim et al., 2021b). Destructive meteotsunamis with a peak-to-trough wave height exceeding 40 cm were detected at the DaeHeuksando (DH), YeongGwang (YG), WiDo (WD), and GunSan (GS) tide gauges (black empty squares in Fig. 1b). Even in meteotsunami events resulting in severe loss of life in the Korean Peninsula, meteotsunami wave heights of just tens of centimeters were recorded at tide gauges. However, according to eye-witness reports, the meteotsunami run-up heights are up to several meters high in coastal areas (Kim et al., 2022). Meteotsunamis exceeding the top 19% of meteotsunami wave heights (40 cm) can be classified as destructive meteotsunamis based on historical meteotsunami events recorded at multiple tide gauges. In addition, we found the co-occurrence of air pressure jumps and meteotsunamis at the DH harbor, where air pressure and sea level observations were performed simultaneously, as shown in Fig. 2. The air pressure disturbance at 10 min intervals (0, 10, 20, 30, 40, and 50 min) was calculated (blue empty circles in Fig. 2a) with air pressure recorded at 1 min intervals based on the above-mentioned real-time monitoring protocol. Along with the low-pressure system,

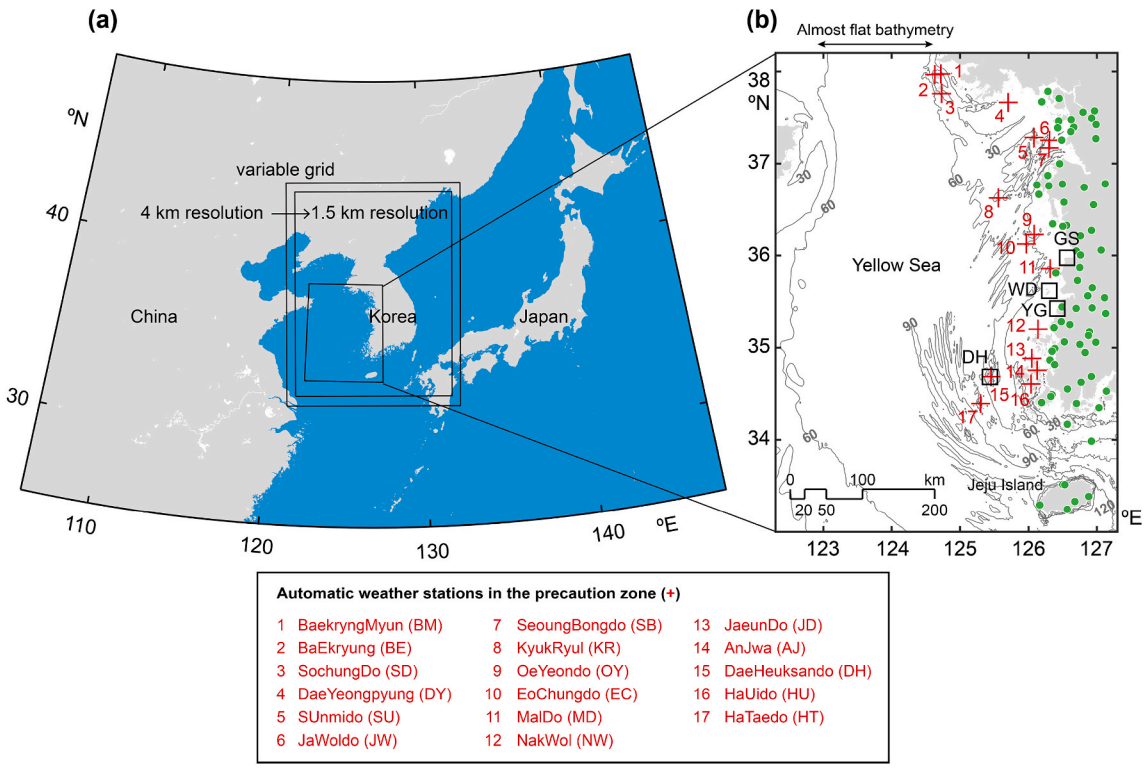


Fig. 1. High-resolution atmospheric model and observation system over the Korean Peninsula. (a) Domain and horizontal resolution of the local data assimilation and prediction system (LDAPS). (b) Bathymetric contours (m) and the observation system consisted of 89 automatic weather stations (AWSs), 17 AWSs in the precaution zone (red crosses), and 72 AWSs in the warning zone (green circles). Strong meteotsunami wave heights (>40 cm) were detected at four tide gauges (black empty squares) on March 4, 2018: GunSan (GS), WiDo (WD), YeongGwang (YG), and DaeHeuksando (DH). A list of the AWSs in the precaution zone (number, full name, and abbreviation) has been provided in the lower part of the figure. (For interpretation of the references to color in this figure legend, the reader is referred to the Web version of this article.)

box-like air pressure oscillations during 1 h (black line in Fig. 2a) were recorded after the onset of the event (E). Two air pressure disturbances nearly twice the intensity threshold for an air pressure jump appeared at 18:50 and 19:20 KST. The air pressure jumps caused the Proudman resonance, as they propagated with similar speed and direction as long ocean waves based on the monitoring reports on March 4, 2018 (Kim et al., 2021a). The speed ratio between the air pressure jumps and the long ocean waves was approximately 0.8. In particular, the pre-amplified long waves locked to the air pressure oscillations sequentially generated seiche excitations in multiple harbors along the propagation path of the air pressure oscillations. Seiche oscillations were characterized by magnitudes (meteotsunami wave heights) of 25–50 cm and resonant periods of less than 30 min. The eastern coast of the Yellow Sea is known as a "harbor meteotsunami" dominated environment, and meteotsunami-induced coastal flooding has been frequently reported every year in the spring season (Kim et al., 2021b).

2.3. Observation and monitoring system

To detect the propagating air pressure jumps from China across the Yellow Sea, the KMA utilizes 1 min mean sea level pressure observations at 89 AWSs (Fig. 1b). By detecting air pressure jumps in advance, the monitoring system on the Korean Peninsula provides early warnings of the occurrence of a meteotsunami. The early warning system for meteotsunamis operated by the KMA is shown in Fig. 3a.

1. Observation: Air pressure jumps were monitored in real-time at 17 AWSs on offshore islands at least 20 km away from the coastline (red crosses in Fig. 1b). In addition, weather radar is used because of the high correlation between the intensity of the rain rate (i.e., radar reflectivity) and air pressure disturbance (Wertman et al., 2014). The radar covers all 89 AWSs and parts of the eastern Yellow Sea, approximately 200 km from the coastline.
2. Forecasting: The monitoring operators predict the possibility of meteotsunamis using the intensity of air pressure jumps detected in the precaution zone and the propagation direction of the cluster of rain rates (>5 mm/h) on the radar. As an observation-based forecast, a lead time of approximately 1 h is expected, although it depends on the propagation pattern of the air pressure jumps.
3. Detection–Warning–Response: When the air pressure jump in the precaution zone propagates into the warning zone (near the coastline), the central KMA provides an early warning of meteotsunami risk to the KMA in each region, coast guard, and local government via a short messaging service (SMS), fax, and hotline.

However, problems such as insufficient lead time have been reported in the case of a specific propagation pattern of air pressure jumps during the test operation of an early warning system (Kim et al., 2022). Occasionally, the monitoring operators need to identify when and where the meteotsunamis would propagate with limited information throughout the forecasting phase of the meteotsunami warning system (17 AWSs and radar observations). This study investigated whether the LDAPS, a high-resolution atmospheric model operated by the KMA, could be used as an early warning system to address reported problems.

2.4. LDAPS

The KMA operates the LDAPS to prepare for the wide or local natural hazards on the Korean Peninsula during each season. As shown in Fig. 1a, the LDAPS uses a horizontal variable grid (inner grid resolution: 1.5 km, outer grid resolution: 4 km) with a model domain covering East Asia (China, Korea, and Japan). It consists of 70 vertical layers up to a

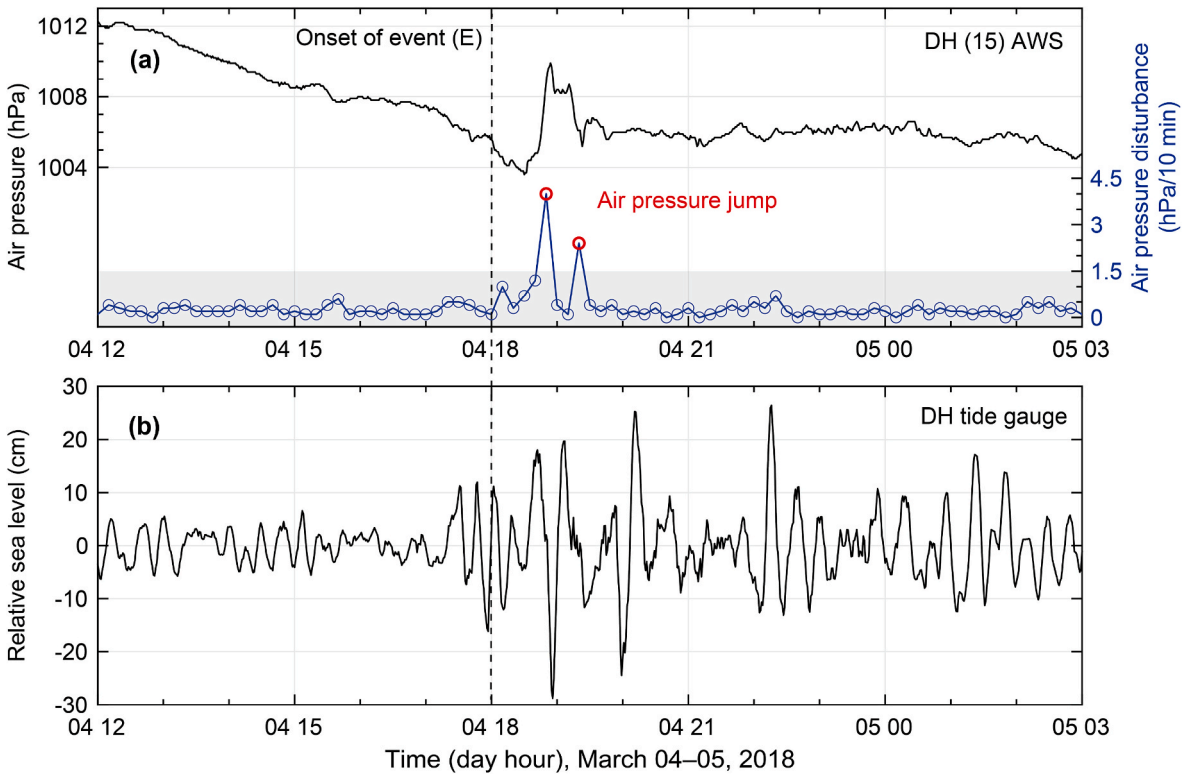


Fig. 2. (a) Air pressure, air pressure disturbance, and air pressure jump at the DH (15) AWS in the precaution zone during the pressure-forced meteotsunami event on March 4, 2018. The gray shaded area highlights the intensity of air pressure disturbance below the limit of air pressure jump (1.5 hPa/10 min). Red circles indicate the detection of air pressure jumps. (b) Sea level oscillations in the meteotsunami frequency band (2 h high-pass filtered) at the DH harbor tide gauge. The black dashed line indicates the onset of the pressure-forced meteotsunami event (E). (For interpretation of the references to color in this figure legend, the reader is referred to the Web version of this article.)

top layer of approximately 40 km, and the dimensions of each horizontal grid are 622 × 810, 1,188 × 1,148. The horizontal and vertical grid systems utilized the Arakawa C-grid, and Charney-Phillips staggered grid systems, respectively (Wang et al., 2020). After the quality control process, the LDAPS uses a three-dimensional variational (3DVAR) data assimilation scheme to select surface and upper air observation datasets. In this scheme, observations around the initialization time are collected and regarded as if they were observations at the initialization time. The pre-processed observational data were utilized in the data assimilation system with a resolution of 3 km. The available data are different over time and space, and although it depends on pre-processing and quality control results, mainly sonde, surface, and aircraft data showed a utilization rate of over 70%. In this study, we used the mean sea level pressure, similar to the pressure observation data predicted by the LDAPS, for its predictability assessment in the early warning system. According to operational efficiency, official predictions are provided with an output time interval of 1 h. However, official outputs are not saved at a sufficiently high frequency to be used as input forcing for meteotsunami generation by sudden air pressure disturbance (Denamiel et al., 2019; Mourre et al., 2021). To capture the air pressure disturbance observed as sudden air pressure changes for several minutes in the time domain (Fig. 2a), an output time interval of 10 min of LDAPS-predicted air pressure was used. This output time interval of the LDAPS predictions is available only for the KMA internal system. Because the interval is the same as the FTP download response time of the real-time monitoring system, it is possible to determine the possibility of using LDAPS data in the current early warning system (Fig. 3a). The KMA conducts 36 h LDAPS predictions at 03, 09, 15, and 21 KST (Korean Standard Time, UTC + 09 h). In this study, to assess the predictability of the LDAPS pressure data, LDAPS predictions (E – 21 h, E – 15 h, and E – 09 h), which were predicted before the onset of the pressure-forced meteotsunami event on March 4, 2018 (E), were compared (Fig. 3b). The prediction (E – 03 h) just before the onset of the event (E) was excluded from the comparison, considering the spin-up time of the LDAPS.

3. Results and discussion

3.1. Air pressure jump detection capability of LDAPS predictions

3.1.1. Propagation pattern of LDAPS prediction

The propagation pattern of the resultant meteotsunamis can be estimated by following the traveling air pressure disturbances for an early warning of the meteotsunamis (Šepić and Vilibić, 2011; Vilibić et al., 2016). We analyzed the horizontal distribution of the surface pressure field of a recent prediction (E – 09 h) to examine LDAPS performance based on simulated propagation (Fig. 4a). In the surface pressure field, a low-pressure system (1,000–1,005 hPa at the center) with a discontinuous pattern located at its edge (dashed circles in Fig. 4a) landed on the west coast of the Korean Peninsula from China across the Yellow Sea. Eq. (1) was used for each grid to filter out the spatial and temporal evolution of air pressure disturbances (i.e., discontinuous patterns) before and after the onset of the event (E). Consequently, the low-pressure system was removed from the simulated pressure field. A cluster of air pressure jumps propagated in the same order as the observed order of meteotsunamis at the DH, WD, YG, and GS tide gauges (Fig. 4b). In addition, we found similar spatial scales and propagation patterns between the clusters of air pressure jumps (Fig. 4b) and rain rates above 5 mm/h (Fig. 4c) based on the correlation between the intensity of rain and air pressure anomalies, as mentioned above. Overall, the cluster of air pressure jumps from the LDAPS prediction arrived more slowly than the observed rain rate on the radar; nevertheless, the simulated spatiotemporal propagation pattern was

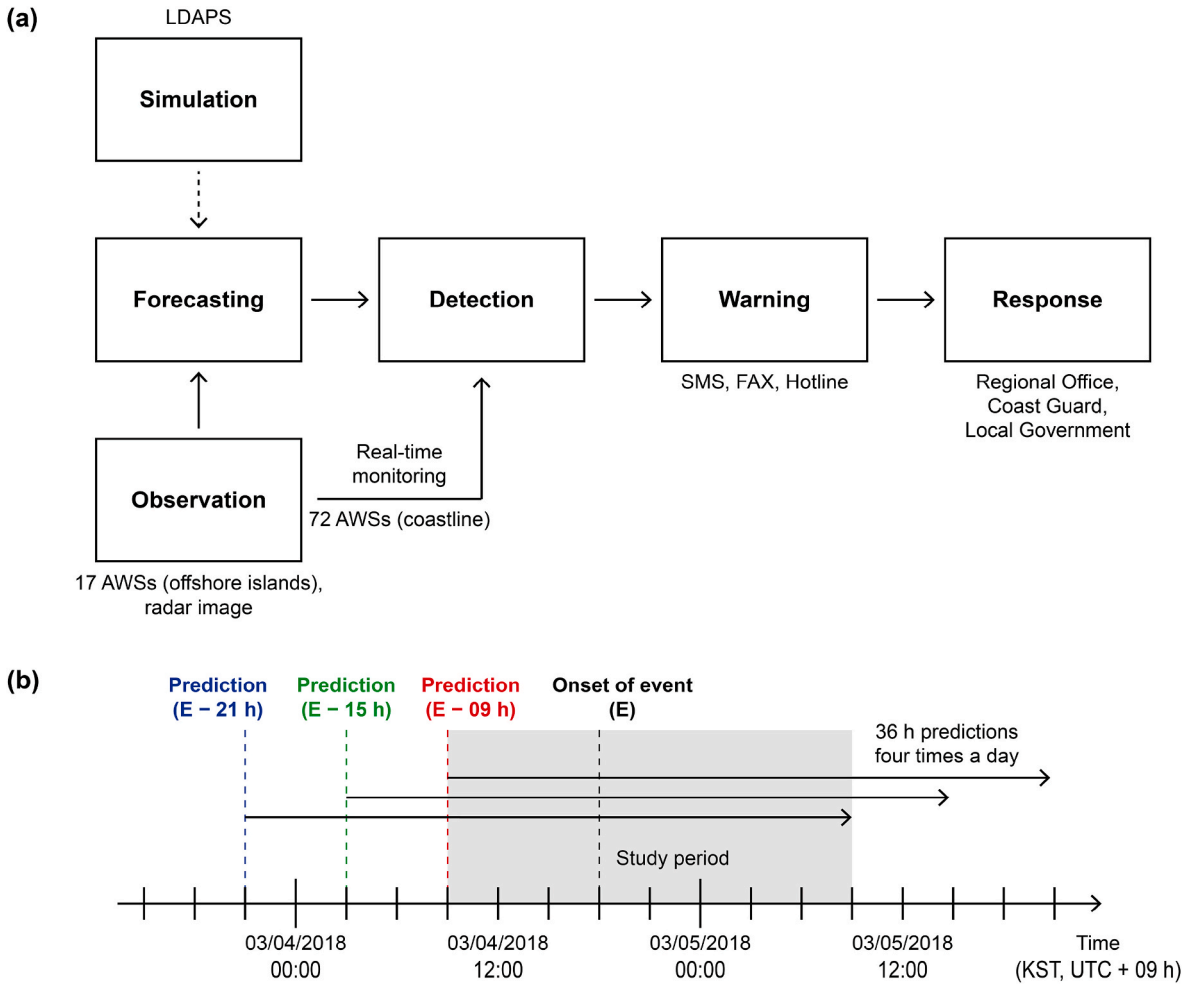


Fig. 3. (a) Early warning system for meteotsunamis and (b) LDAPS predictions (E – 21 h: blue, E – 15 h: green, E – 09 h: red) before the onset of the meteotsunami event (E) at 18:00 KST on March 4, 2018. (For interpretation of the references to color in this figure legend, the reader is referred to the Web version of this article.)

reasonable.

3.1.2. *Evaluation of LDAPS air pressure*

The air pressure at the 17 AWSs in the precaution zone is of utmost importance (Kim et al., 2021a) for the observation-forecasting phase of the early warning system (Fig. 3a). The accuracy of the LDAPS in predicting air pressure was evaluated to assess the possibility of using the simulated air pressure in the warning system. The LDAPS inner grid covering the Korean Peninsula has a high horizontal resolution of $1.5 \times 1.5\ km^2$ (Fig. 1a), and the minimum distance between AWSs in the precaution zones is approximately 8 km (Fig. 1b). Accordingly, LDAPS does not have a grid cell with two or more AWSs. We evaluated the simulated air pressure (E – 21 h, E – 15 h, and E – 09 h) using the nearest grid point in the model grid cell from each AWS. Fig. 5a depicts the actual and expected time series of the four AWSs in the precaution zone, where large air pressure jumps were noted. The low-pressure system was accompanied by high-frequency peaks that increased up to several hPa in a few minutes. The long-term trends of the predicted air pressures were overestimated with deviations of 1–4 hPa. The peaks of the shorter-lasting disturbances (i.e., air pressure disturbances) were underestimated and had a time lag of approximately 1–2 h (Fig. 5a), similar to the previous propagation pattern (Fig. 4). In addition, we found that the time resolution (output time interval of 10 min) was insufficient to reproduce the disturbance details. These details play an essential role in the final magnitude of the meteotsunamis. For meteotsunami simulations, atmospheric forcing should be applied every minute to capture the intensity of disturbances (Denamiel et al., 2019).

The general performance of the LDAPS predictions in the precaution zone was assessed using the Taylor diagram (Fig. 5b), which presents the analysis of normalized standard deviations and cross-correlations from 9:00 KST on March 4 to 9:00 KST on March 5. The statistical validation results for each prediction were not significantly different. The simulated air pressure indicated high predictability, with a correlation coefficient of more than 0.9 and a centered root mean square difference of less than 0.5. However, a correlation more significant than 0.9 mainly represents the correlation of the low-frequency parts (>5 h), as shown in Table 1. The correlation of the high-frequency parts (<5 h), which are relevant for meteotsunami generation, is less than 0.5 for the four AWSs. Owing to the time lag of the LDAPS air pressure, it was difficult to assess which LDAPS best predicted the simulated air pressure disturbances based on the time series and Taylor diagrams.

3.1.3. *Intensity and arrival time of LDAPS air pressure jump*

To quantitatively compare the detection capability of the LDAPS prediction, air pressure disturbances were calculated using the air pressure anomalies from 18:00 to 21:00 KST on March 4, 2018 (Fig. 5a), in the same manner as the current monitoring protocol, at the 17 AWSs in the precaution zone (Fig. 6). As traveling air pressure disturbances rapidly lose their energy by dissipation on land, the accurate detection of the intensity and arrival time at outer AWSs is crucial for early warning. The maximum air pressure jumps ranging from 1.6 to 6.4 hPa/10 min were observed at the 6 AWSs located south of the precaution zone from the HT (17) to NW (12) AWSs (black label in Fig. 6a). In contrast, only one pressure jump was simulated in Prediction (E – 21 h), and no

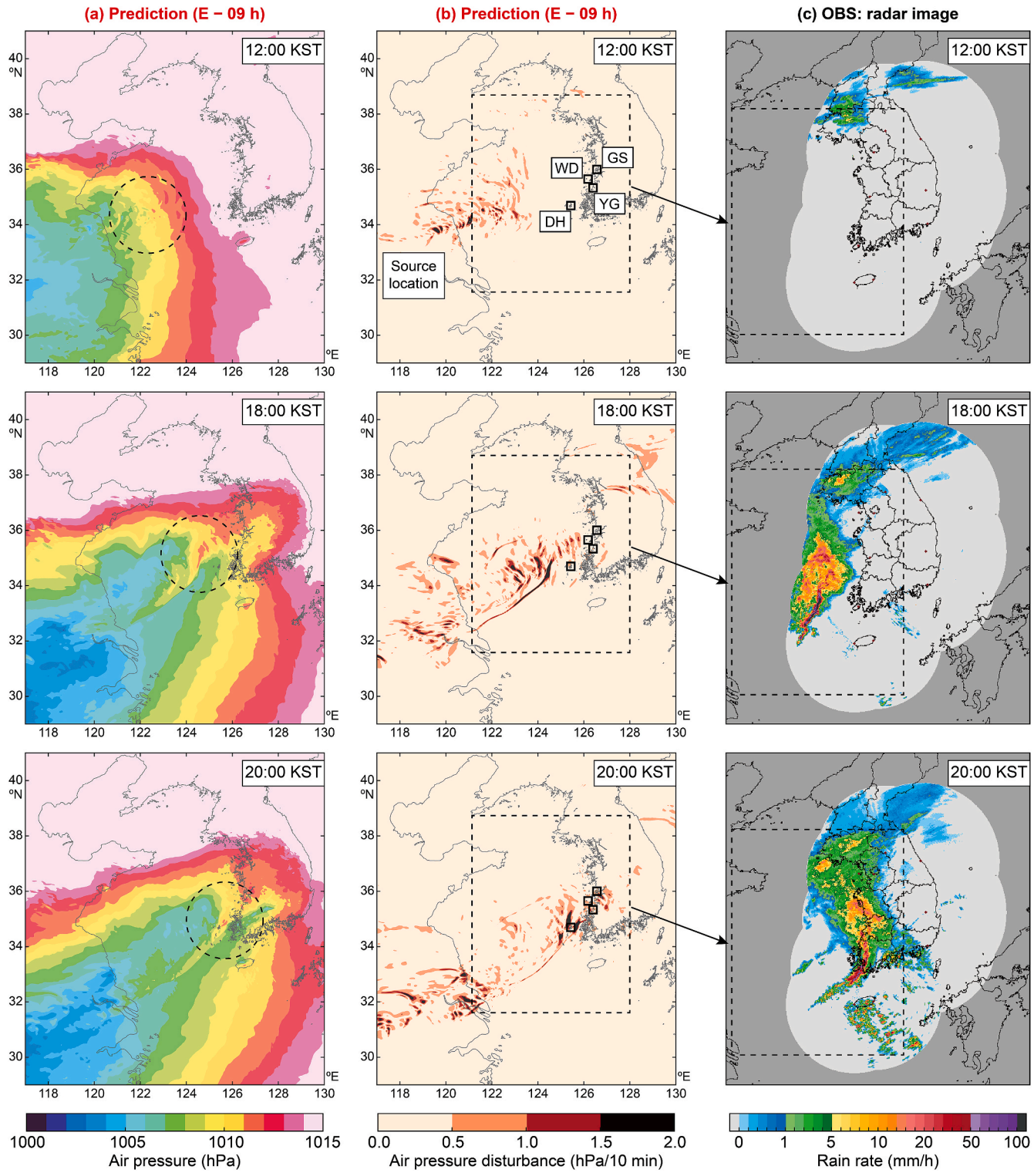


Fig. 4. Snapshots of atmospheric disturbances at 12:00, 18:00, and 20:00 KST on March 4, 2018. (a) Predicted air pressure (E – 09 h). The dashed circles enclose the area with air pressure disturbances. (b) Calculated air pressure disturbance using the LDAPS prediction (E – 09 h). The black empty squares indicate the tide gauges where strong meteotsunamis were detected. The dashed box encloses the shared area between the LDAPS domain and radar coverage along the west coast of the Korean Peninsula. (c) Observed rain rate in radar images. (For interpretation of the references to color in this figure legend, the reader is referred to the Web version of this article.)

pressure jump was simulated in the next Prediction (E – 15 h), as shown in Fig. 6b and c. The arrival order of the simulated air pressure disturbances (E – 21 h and E – 15 h) did not match the observation-based results (OBS: 17 AWSs), even when considering the underestimation of the pressure anomalies in the LDAPS predictions (Fig. 5a–c). Among the LDAPS predictions, Prediction (E – 09 h) simulated the air pressure disturbance with the most similar intensity to that observed (Fig. 5a and d). In particular, the arrival order of the simulated air pressure jumps at the AWSs agrees well with the AWS observations. From the perspective of the performance of the LDAPS prediction (E – 09 h), the simulated

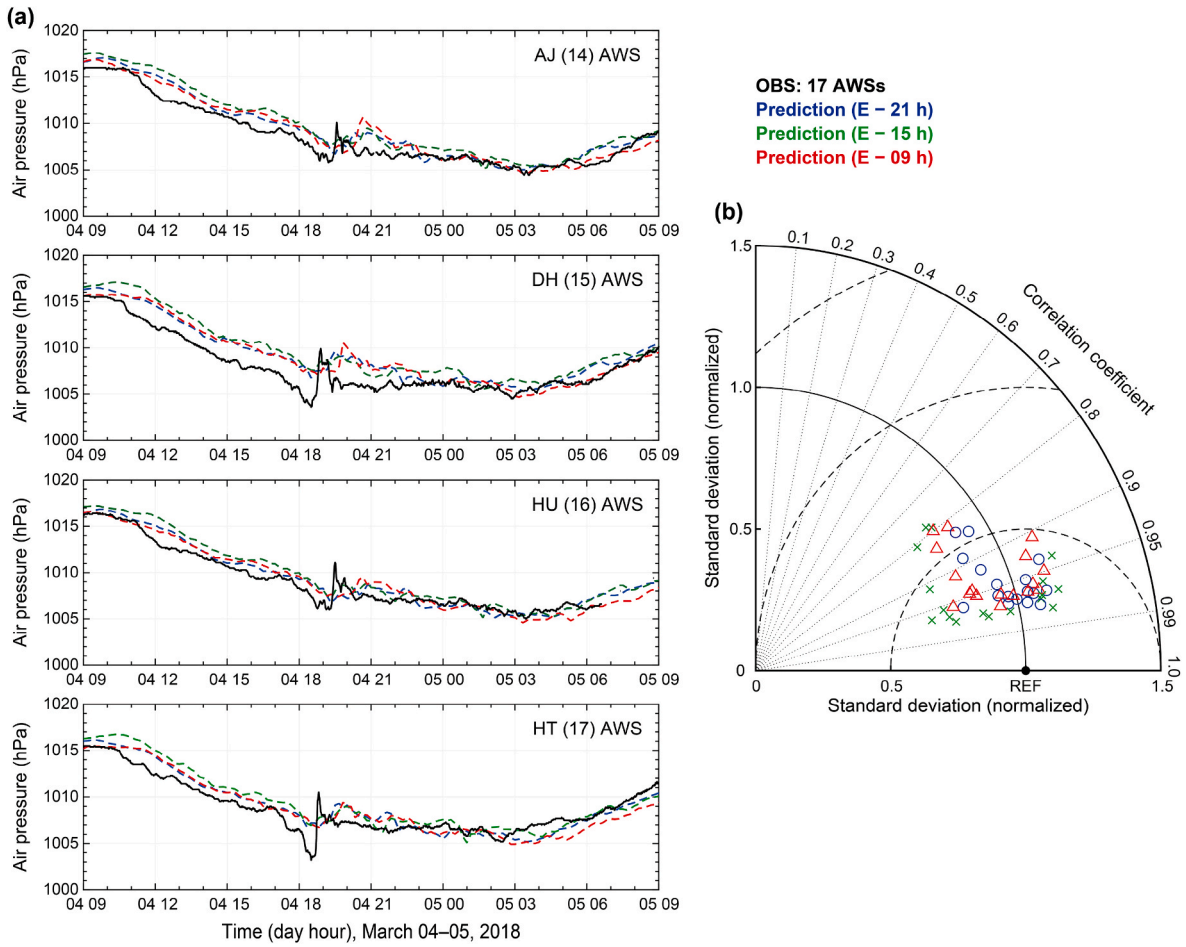


Fig. 5. (a) Time series comparison of observed and predicted air pressure at four AWSs in the precaution zone, where the strongest air pressure jumps were detected, and (b) Taylor diagram illustrating LDAPS performance for each prediction time compared to observed air pressure at 17 AWSs in the precaution zone. (For interpretation of the references to color in this figure legend, the reader is referred to the Web version of this article.)

Table 1
Correlation coefficients for low- and high-frequency parts (5 h cut-off period) of observed and predicted air pressure at 17 AWSs in the precaution zone.

17 AWSs (precaution zone)	Low-frequency part			High-frequency part		
	Prediction (E – 21 h)	Prediction (E – 15 h)	Prediction (E – 09 h)	Prediction (E – 21 h)	Prediction (E – 15 h)	Prediction (E – 09 h)
BM (01)	0.87	0.81	0.83	0.25	0.31	0.35
BE (02)	0.86	0.80	0.82	0.22	0.34	0.45
SD (03)	0.91	0.83	0.87	0.53	0.34	0.10
DY (04)	0.93	0.94	0.93	0.02	0.03	0.06
SU (05)	0.96	0.96	0.95	0.09	0.31	0.11
JW (06)	0.97	0.98	0.96	0.12	0.23	0.17
SB (07)	0.97	0.98	0.95	0.17	0.09	0.16
KR (08)	0.97	0.97	0.96	0.10	0.15	0.21
OY (09)	0.98	0.99	0.97	0.11	0.29	0.63
EC (10)	0.98	0.98	0.98	0.32	0.36	0.65
MD (11)	0.98	0.98	0.97	0.20	0.58	0.66
NW (12)	0.97	0.98	0.96	0.40	0.39	0.54
JD (13)	0.98	0.98	0.97	0.12	0.17	0.08
AJ (14)	0.99	0.99	0.98	0.04	0.31	0.05
DH (15)	0.97	0.97	0.95	0.15	0.43	0.06
HU (16)	0.98	0.98	0.98	0.08	0.34	0.03
HT (17)	0.96	0.96	0.94	0.16	0.38	0.12

result of the air pressure jump (Fig. 6d) can be summarized as follows: (i) the late arrival of the air pressure jump by approximately 1 h and (ii) the underestimation of the intensity of the air pressure disturbance by 40% (1.5–2.6 hPa/10 min).

3.2. Application of LDAPS for an early warning system

The KMA issued a meteotsunami warning when an air pressure jump propagated from the precaution zone to the warning zone using 89 AWSs (Fig. 3a). Based on the real-time monitoring protocol, we assessed the applicability of the LDAPS Prediction (E – 09 h) for early warning by

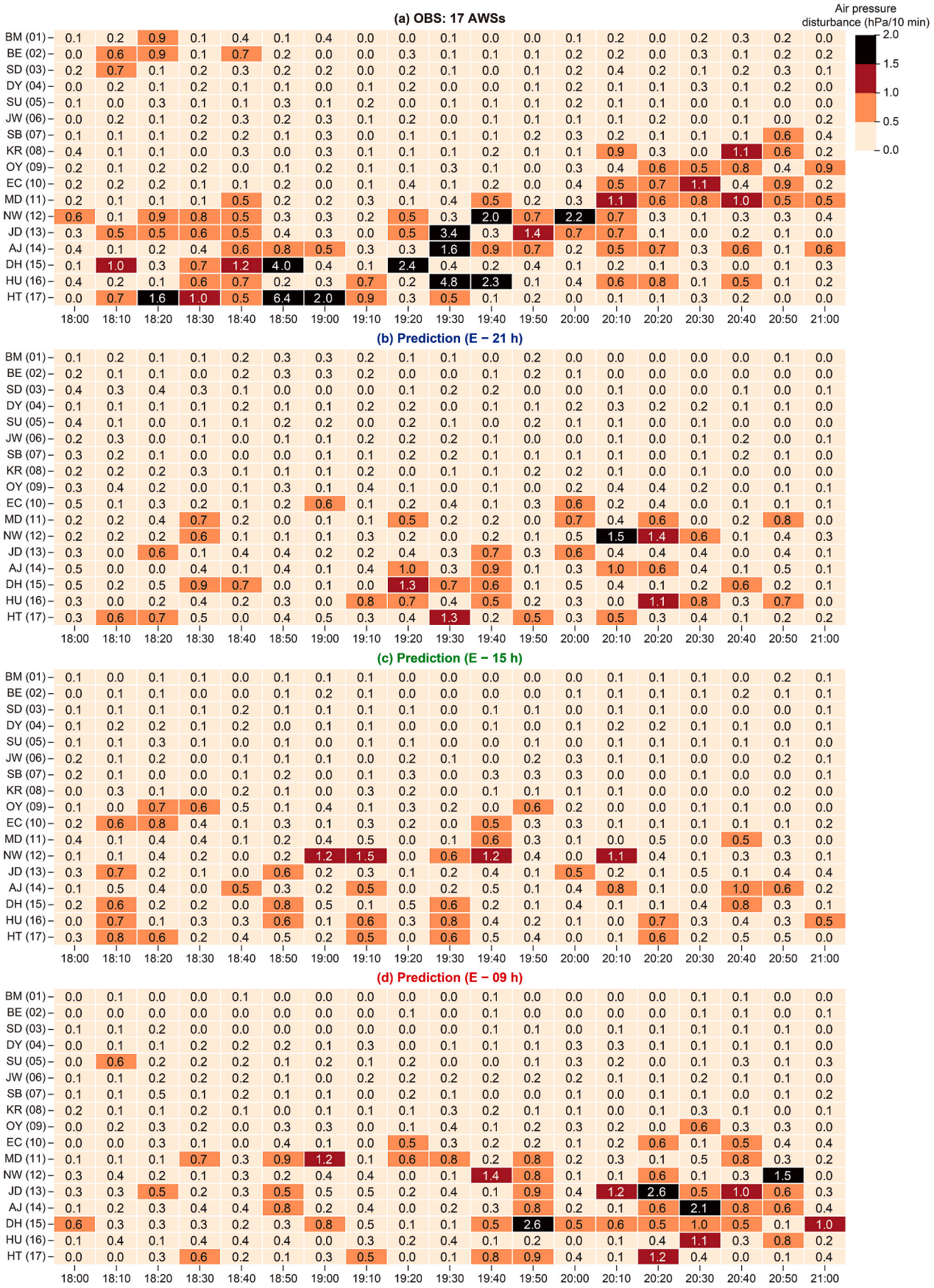


Fig. 6. Comparison of (a) observed and (b–d) predicted air pressure disturbance during the meteotsunami event at 17 AWSs in the precaution zone (see Fig. 1b red crosses). (For interpretation of the references to color in this figure legend, the reader is referred to the Web version of this article.)

comparing the propagation patterns of the simulated and observed air pressure jumps. Fig. 7 shows the propagation map and maximum intensity of the air pressure jump from 18:00 to 22:00 KST on March 4, 2018, using the LDAPS Prediction (E – 09 h) and observation system. According to the predicted and observed results (Fig. 7), the main propagation of the air pressure jumps toward the Korean Peninsula is consistent with the arrival pattern of the resultant meteotsunamis (Fig. 1b). The detection rate (agreement ratio between the simulated and observed air pressure jump detections) for each zone was 67% (4/6) in the precaution zone and 25% (5/20) in the warning zone. Similar to the previous results, the detection rate for each zone seemed to be low because the simulated air pressure disturbances were underestimated. In particular, the intensity of the simulated air pressure disturbances appeared to dissipate faster than that observed in the warning zone along the coastline.

As mentioned above, the KMA has operated an observation-based monitoring system with insufficient lead time. This lead time issue will be addressed by supporting the current early warning system if the propagation pattern of air pressure jumps is estimated in advance through LDAPS model-based forecasting. The pre-amplified long waves (ζ_P) due to the Proudman resonance (Monserrat et al., 2006; Proudman, 1929) can be approximated by monitoring the propagation characteristics of the predicted air pressure jump in the open sea.

$$\zeta_P \approx \frac{\Delta\overline{\zeta}c^2}{c^2 - U^2} = \frac{\Delta\overline{\zeta}}{1 - Fr^2} \tag{2}$$

where $\Delta\overline{\zeta} = -\Delta P_a/\rho g$ is the inverted barometer response at sea level, ΔP_a is the air pressure disturbance, ρ is the water density, g is the acceleration due to gravity, U is the speed of the air pressure jump, c is the long-wave phase speed, and Fr is the Froude number ($Fr = U/c$). The long-wave phase speed ($c = \sqrt{gh}$) is determined by the corresponding bottom depth (h), where the cluster of the air pressure jump propagates. Monitoring the intensity (ΔP_a) and speed (U) of air pressure disturbances is crucial for early warning of the magnitude of resonant waves in the open sea. In addition, a certain depth range where air pressure disturbances travel in the open sea should be monitored to estimate the Froude number (Fr). It is important to know the full matching of the speeds ($Fr \approx 1$) along the disturbance path because the Proudman resonance strongly depends on the range of the Fr (Vilibić, 2008).

We diagnosed the possibility of an early warning by tracking the propagation pattern (propagation path and speed range) of the simulated air pressure jumps beyond the observation coverage (Fig. 8). From noon on March 4, 2018, clusters of air pressure disturbances below the limit of the air pressure jump propagated toward the open Yellow Sea from the source location in eastern China (Fig. 4b). The evolution of the air pressure jump that developed in a y-shaped structure from 15:00 to 20:00 KST was tracked based on hourly monitoring (red scatters in Fig. 8). The meteotsunami hazard area derived from the simulated propagation path was consistent with that determined by observation points where air pressure jumps, and meteotsunamis were detected together. Subsequently, the cores of the air pressure jumps (black scatters in Fig. 8) were tracked along the propagation path to estimate the speed of the complex y-shaped structure. It is assumed that the speed of the cores of the air pressure jumps represents the speed of the complex structures of air pressure jumps. The cores of the air pressure jumps were defined as scatter points exceeding the 99 percentile of the air pressure jump intensity from the source location to the observation system (>4.0 hPa/10 min). As a result, the cores of the air pressure jumps appeared from 16:00 to 18:00 KST, and their hourly intensities are presented in Table 2. The mean and maximum intensities of the air pressure jump cores maintained a constant level during propagation. Interestingly, the core count was well developed at 17:00 KST within the depth range corresponding to a long-wave phase speed of 25–30 m/s. The speed range of the air pressure jumps calculated using the centroids of the cores (U_{core}) was 24–30 m/s, approximating the long-wave phase speed of the corresponding depth. The estimated Fr with the LDAPS prediction ranged from 0.8 to 1.2, corresponding to the Proudman resonance and near-resonant conditions (Vilibić, 2008). Moreover, the area traveled by the cores of the air pressure jumps (black vectors in Fig. 8) was characterized by a gentle bottom slope (Fig. 1b), which can maintain consistent resonant conditions. The applicability of the LDAPS prediction for the early warning was assessed by monitoring favorable conditions of air pressure jumps for meteotsunami generation in the open sea.

As shown in Fig. 3a, the current early warning of meteotsunami is

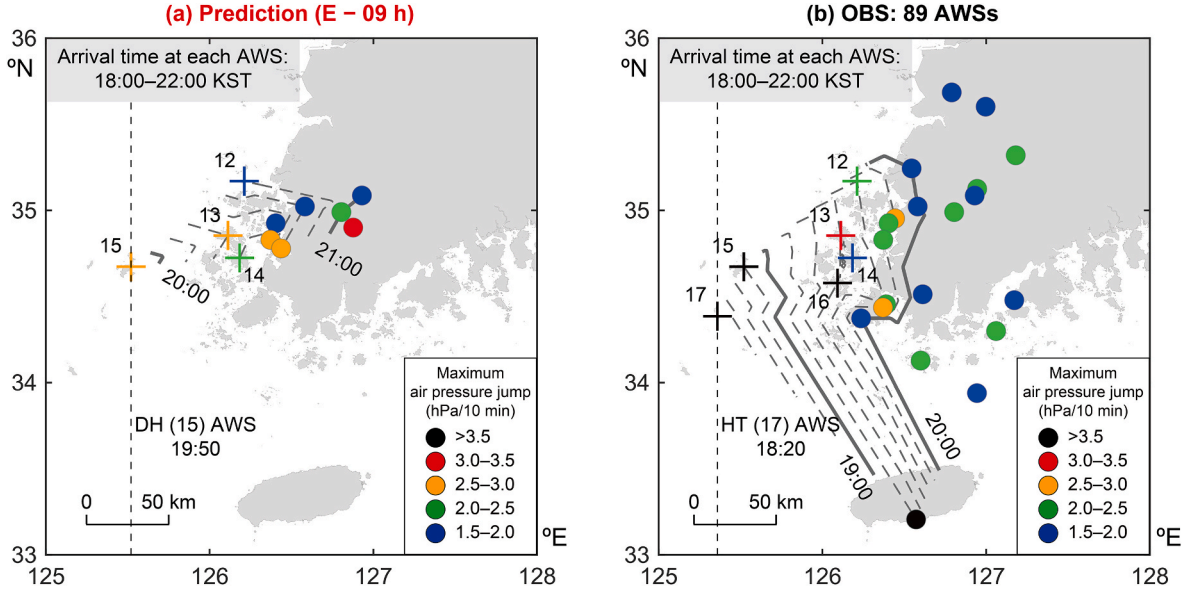


Fig. 7. Propagation pattern of air pressure jump using (a) LDAPS prediction (E – 09 h) and (b) that observed at 89 AWSs, based on the real-time monitoring protocol. The thick and dashed gray lines indicate isochrones of the air pressure jump (1 h and 10 min) calculated from the arrival time list from 18:00 to 22:00 KST on March 4, 2018, and the locations of each AWS, respectively. The colors of the circles indicate the maximum intensity of the air pressure jump. The black dashed line indicates the AWS where the first air pressure jump arrived. (For interpretation of the references to color in this figure legend, the reader is referred to the Web version of this article.)

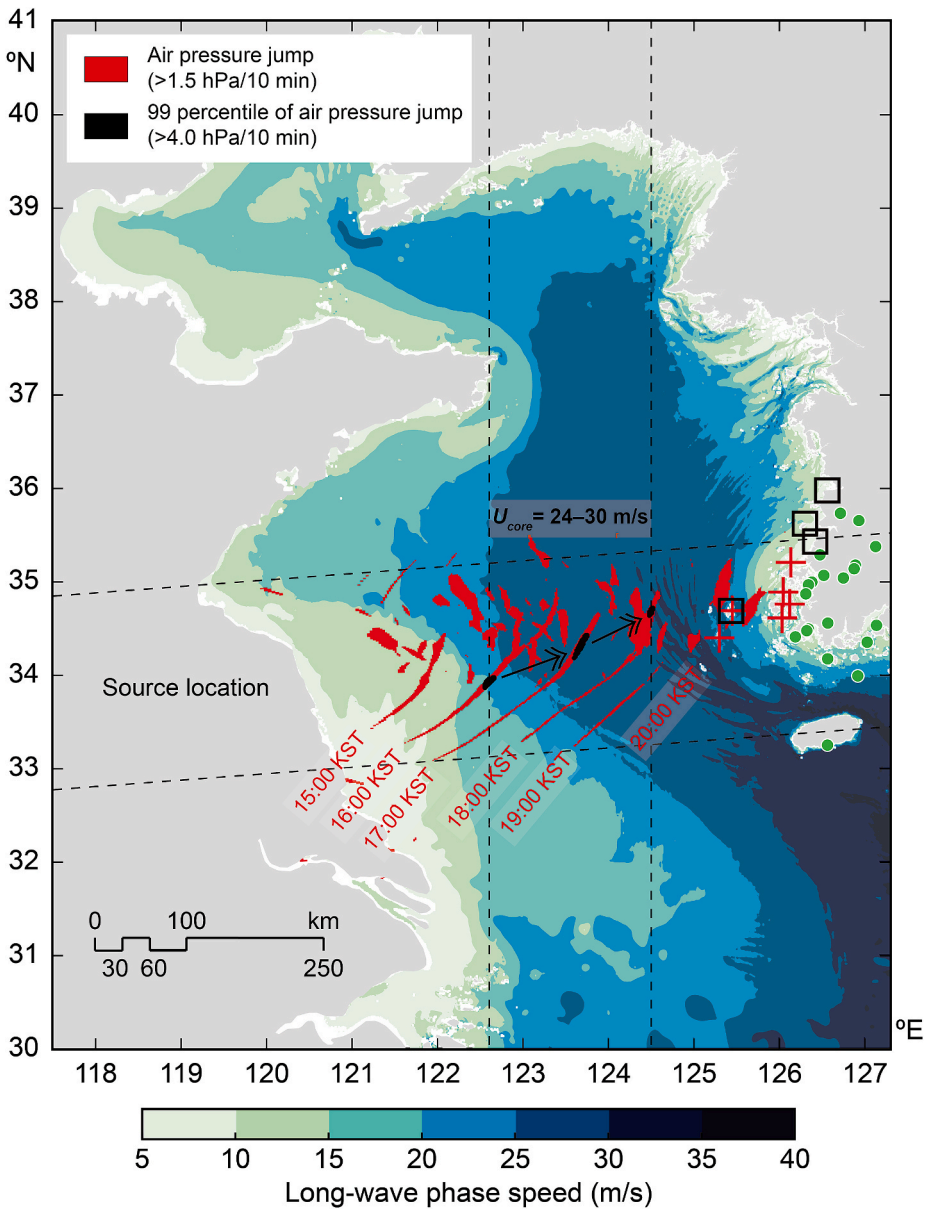


Fig. 8. Application of LDAPS prediction (E – 09 h) in early warning system from 15:00 to 20:00 KST on March 4, 2018. Graded colors on the map denote the long-wave phase speed of the Yellow Sea. The horizontal grid lines indicate the propagation path of hourly air pressure jumps (red scatters) and 99 percentile (i.e., core) of air pressure jumps (black scatters). The vertical grid lines and the black vectors represent a traveled area of core of air pressure jumps in the open sea. The markers (red crosses, green circles, and black empty squares) indicate the observation points where air pressure jumps (see Fig. 7b) and the resultant meteotsunamis (see Fig. 1b) were detected. (For interpretation of the references to color in this figure legend, the reader is referred to the Web version of this article.)

Table 2
Intensity of 99% percentile of predicted air pressure jump from 16:00 to 18:00 KST on March 4, 2018 (see Fig. 8).

Time (KST)	Core count	Mean	Maximum
16:00	31	4.3	4.6
17:00	45	4.2	4.5
18:00	16	4.3	4.5

issued in the detection phase based on real-time monitoring of 89 AWSs and weather radar. A new early warning system can be issued based on observations and an atmospheric model-based warning system. The contribution of LDAPS prediction is not an alternative but a complementary role of the observation-based monitoring system in providing a timely meteotsunami warning. In the forecasting phase, the LDAPS prediction enables an earlier warning for (i) meteotsunami hazard areas assessed from the propagation path of the air pressure jump and (ii) a favorable speed range for the Proudman resonance in the open sea (Fig. 8). For a more accurate warning, monitoring operators can issue warnings only when the simulated air pressure jumps in the precaution zone coincide with the location of the observed air pressure jumps in the precaution zone (Fig. 7). Accordingly, a sufficient lead time can be ensured because the monitoring operators do not wait for air pressure jump detection in the warning zone. Considering the 36 h prediction and a prediction interval of 6 h (Fig. 3b), the LDAPS time lag of approximately 1 h, as mentioned above, does not pose a significant problem for sufficient lead time. Monitoring operators must carefully examine the evolution and dissipation of the simulated air pressure jump during propagation in the open sea. In addition, it is necessary to check whether the direction and speed range correspond to the dangerous conditions of historical meteotsunami events along the west coast of the Korean Peninsula (Kim et al., 2021b).

3.3. *Predictability of meteotsunamis with 10 min LDAPS*

3.3.1. *Sensitivity of air pressure disturbance by output time interval*

The meteotsunami warning system presented in this study is characterized by sending warning SMSs of meteotsunami occurrences with an observation-based monitoring system (Kim et al., 2021a). Additionally, in a future study, atmosphere-ocean coupled modeling should be

performed to prepare for potential false alarms because of the interference and amplification of observations on the west coast of the Korean Peninsula. The simulation of forced long waves, generated by continuous energy pumping from traveling air pressure disturbances in the open sea, is shown in Eq. (2) and is sensitive to the output time interval of an atmospheric model (Mourre et al., 2021). Moreover, the magnitude of the final resonance in harbors or over the continental shelf can be determined by reproducing detailed air pressure disturbances (Denamiel et al., 2019). The suitability of the output time interval for the atmospheric model likely depends on the geometry of the affected harbors or coastal areas. In the Korean Peninsula, 88% of the meteotsunamis have less than 30 min dominant period bands due to meteotsunami-induced harbor seiches (Kim et al., 2021b). In particular, 57% of the wave periods were distributed between 10 min and 20 min. Under these circumstances, an output time interval of 10 min was insufficient to represent the details of the disturbances in the time domain (Fig. 5a). Intense air pressure disturbances can occur at time scales of 1 min. Our calculation considering air pressure changes over 10 min, allows shorter-lasting disturbances to be smoothed or even removed (Šepić and Vilibić, 2011).

To indirectly assess the sensitivity of the simulated air pressure jump to the output time interval, we compared the temporal resolution of the air pressure disturbances for each analysis interval (Fig. 9). This process was performed using 1 min pressure data at the HT (17) AWS, where the strongest air pressure jump (6.4 hPa/10 min) was observed on March 4, 2018, among all 89 AWSs (Fig. 6a). The comparison of the different analysis intervals (1, 5, and 10 min) was based on the sum of the air pressure disturbances (Fig. 9b–d) from 18:40 to 18:50 KST when the maximum gradient of air pressure oscillations was observed (Fig. 9a). Consequently, the sum of the air pressure disturbances for each analysis interval was almost the same (Fig. 9b–d). However, we found that a shorter output time interval improved the temporal resolution of rapid air pressure oscillation and the accuracy of the arrival time. From the perspective of meteotsunami simulation (i.e., atmosphere-ocean coupled modeling), model errors due to the atmospheric model (ε_{air}) can be divided into two model errors as follows:

$$\varepsilon_{air} = \varepsilon_{mod} + \varepsilon_{out} \tag{3}$$

where ε_{mod} includes the overall errors related to an atmospheric model (such as the initial state, model equations, and model parameterizations), and ε_{out} is the model error due to the sparse output time interval. The output time interval of the current LDAPS prediction (10 min) was estimated to be the minimum output time interval for resolving a sudden air pressure jump. However, it is still necessary to shorten the output time interval in the future by considering the potential ε_{out} owing to the output time interval.

3.3.2. *Wavelength of air pressure oscillation vs. horizontal resolution*

A high-resolution atmospheric model should capture wavelength of box-like air pressure oscillations (Fig. 2a) to predict pressure-forced

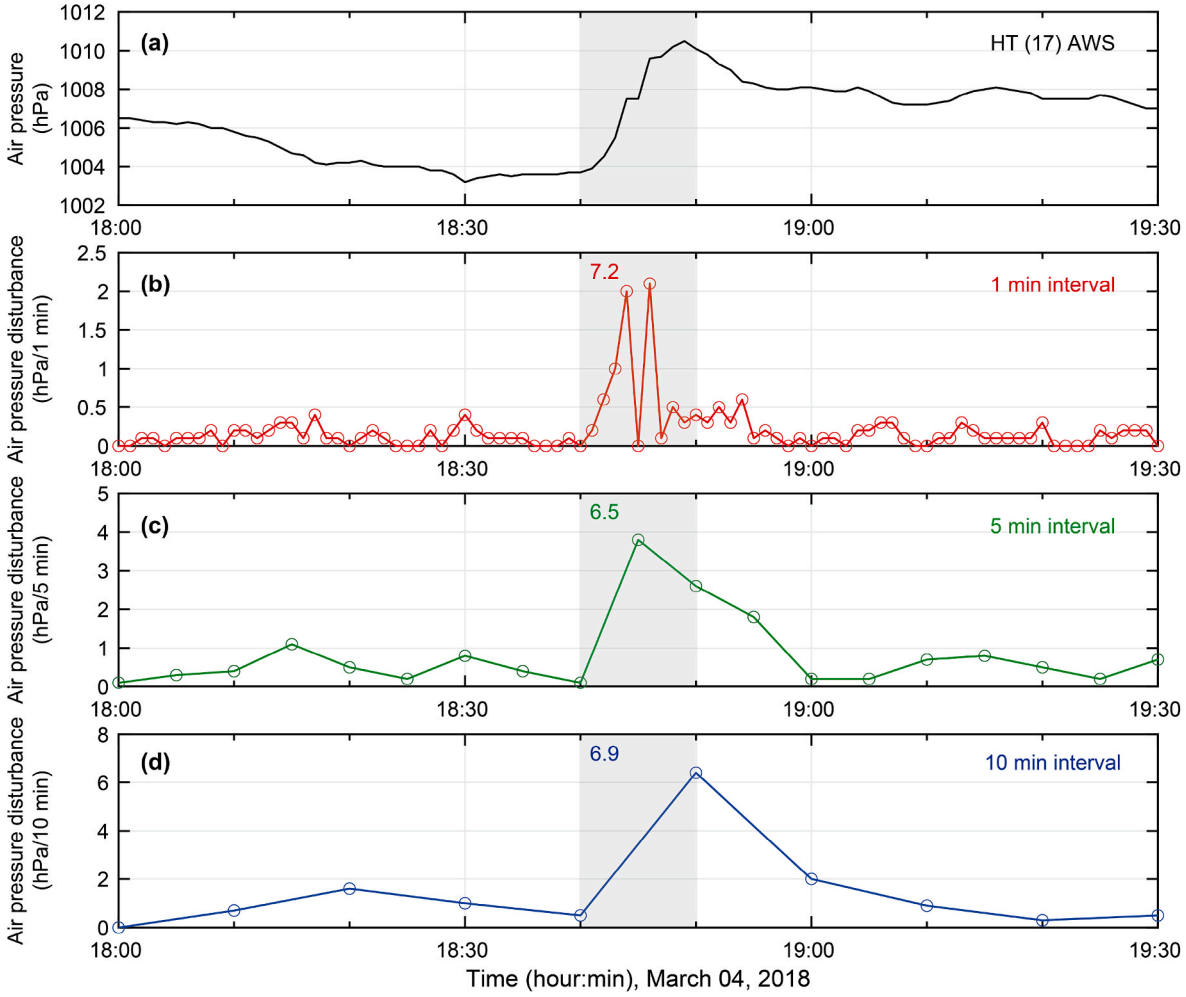


Fig. 9. (a) Observed air pressure at HT (17) AWS in the precaution zone and (b–d) sensitivity of air pressure disturbance for each output time interval. The gray shaded area and number indicate the period when the maximum gradient of air pressure oscillations was observed and the sum of air pressure disturbances during the period, respectively. (For interpretation of the references to color in this figure legend, the reader is referred to the Web version of this article.)

meteotsunamis. As the LDAPS domain (inner grid) covers most of the Yellow Sea area with a horizontal resolution of 1.5 km, the cluster of air pressure disturbances can be found in the simulated surface pressure field (Fig. 4a and b). To examine the number of LDAPS grid points included within the wavelength of the air pressure oscillations more quantitatively, we roughly estimated the wavelength. The estimation of the wavelength was based on the wave period (30 min), assumed as the time difference between the two air pressure jumps at the DH (15) AWS (red circles in Fig. 2a), and the wave speed (24–30 m/s) of the air pressure jump calculated from the LDAPS prediction (Fig. 8). The wavelength of the air pressure oscillation on March 4, 2018, was estimated to be approximately 43–54 km. The range of the wavelengths estimated from multiple observations of pressure data was 20–120 km in other regions (Horvath et al., 2018; Kazeminezhad et al., 2021). Consequently, air pressure oscillations were captured with 29–66 LDAPS grid points. Although it is case-dependent on the waveform and duration of air pressure oscillations, considering the high horizontal resolution of the LDAPS compared to the range of the wavelength, the LDAPS prediction has sufficient resolution to capture air pressure oscillations propagating through the open Yellow Sea.

3.3.3. *Adjustment of surface pressure field for meteotsunami modeling*

This study investigated whether the intensity and propagation pattern of air pressure jumps could be properly reproduced using the LDAPS surface pressure field. It is necessary to consider that short periods of air pressure peaks were underestimated in LDAPS when simulating the meteotsunami phenomenon. In modern meteotsunami research, attempts to create surface pressure fields for meteotsunami modeling can be summarized as follows:

- user-defined surface pressure fields based on meteorological observations (e.g., meteorological network, weather radar, and satellite) characterized by constant air pressure oscillations, such as waveform, duration, source location, speed, and direction (Bechle and Wu, 2014; Kim and Omira, 2021; Ličer et al., 2017; Linares et al., 2016; Perez and Dragani, 2021; Rabinovich et al., 2021; Šepić et al., 2015a; Wang et al., 2021);
- spatially and temporally varying surface pressure fields after simulation using an atmospheric model, which is commonly used in real-time operating systems (Anderson and Mann, 2021; Denamiel et al., 2019; Shi et al., 2019; Tojčić et al., 2021);
- adjusted surface pressure field after simulating an atmospheric model (Huang et al., 2021).

The reconstructed surface pressure field ($RP^t{}_i$) can be post-processed to overcome the underestimation of the air pressure jump in the LDAPS prediction as follows:

$$RP^t_i = \Delta P^t_i \times (AF - 1) + P^t_i \tag{4}$$

where ΔP^t_i is the high-pass filtered air pressure at model grid i and time t, AF is the amplification factor; and $P^t{}_i$ is the simulated air pressure. Based on the adjustment of the pressure anomaly during a short period of air pressure oscillations, the underestimated surface pressure field can be amplified while preserving the long-period air pressure component in the low-pressure system. Note that while the air pressure is adjusted to increase the intensity of air pressure disturbances, the period bands of air pressure oscillations, which significantly affect the determination of the final magnitude of meteotsunamis at coastal locations, cannot be modified. However, it is worth trying this adjustment because the LDAPS reproduced the waveform and propagation pattern of the air pressure oscillations well. To reproduce the propagation and amplification of meteotsunamis in ocean models under realistic conditions, it is necessary to adjust the pressure anomalies presented in this study. This allows monitoring operators to prepare for several meteotsunami hazard scenarios based on surface pressure fields adjusted with optimal AF s.

4. Conclusions

We quantitatively evaluated the detection capability of LDAPS air pressure predictions for widespread and destructive air pressure jumps and meteotsunami events on March 4, 2018. The monitoring results of air pressure jumps using the observation system were compared to the simulated results of LDAPS predictions. Owing to the limitations of the LDAPS predictions, the intensity of the air pressure jump was underestimated by 40%, and there was a time delay of approximately 1 h. In addition, air pressure jumps over a short period (5–10 min) could not be detected with an output time interval of 10 min. Accordingly, there is a question of whether even small-scale air pressure jumps can be captured in space and time. Despite these limitations, we determined the strengths of the LDAPS predictions, which can contribute to the current warning system. The detection rate of the LDAPS air pressure jump was 67% in the precaution zone of the observation system, and the propagation pattern was consistent with real-time monitoring results. In particular, the propagation path and speed range of the air pressure jump favorable to meteotsunami generation could be monitored using LDAPS in the open Yellow Sea, far beyond the observation coverage. This implies that lead time problems in the observation-based warning system can be addressed by applying LDAPS predictions to the warning system. When forecasting the potential of meteotsunamis using the proposed warning system, monitoring operators should select the best LDAPS prediction. It seems better to select LDAPS predictions that simulate relatively strong air pressure disturbances considering the underestimation issue.

The proposed system is suitable for warning about tsunamigenic atmospheric disturbances with an increased lead time compared to observations. Currently, the KMA is preparing to quantitatively predict the intensity of meteotsunamis over the Korean Peninsula by operating an atmosphere-ocean coupled model. The LDAPS with a horizontal resolution of 1.5 km covering the entire Yellow Sea was confirmed to be suitable for capturing the wavelength and propagation of air pressure oscillations. However, the output time interval of 10 min is not sufficient to model meteotsunamis, which involves final harbor amplification sensitive to the details of the air pressure oscillations. The Korean Peninsula is a harbor meteotsunami-dominated environment, favorable for amplification around resonant periods of less than 30 min. Therefore, it is necessary to check whether resonant waves can be reproduced in the open sea with 10 min of atmospheric forcing. If possible, the output time interval should be reduced to 1 min to capture the rapidly fluctuating air pressure over short periods accurately. A simple approach can bypass the underestimation of short periods of air pressure peaks, such as adjusting the simulated surface pressure field when performing LDAPS-based meteotsunami modeling.

CRediT authorship contribution statement

Myung-Seok Kim: Conceptualization, Methodology, Formal analysis, Writing – original draft.

Seung-Buhm Woo: Conceptualization, Writing – review & editing, Project administration, Funding acquisition.

Hyunmin Eom: Conceptualization, Methodology.

Sung Hyup You: Project administration, Funding acquisition.

Hye Min Lee: Data curation, Validation.

Declaration of competing interest

The authors declare that they have no known competing financial interests or personal relationships that could have appeared to influence the work reported in this paper.

Acknowledgments

The authors would like to thank two anonymous reviewers for their

helpful suggestions. This work was supported by Institute of Information and Communications Technology Planning and Evaluation (IITP) grant funded by The Korean Government (MSIT) (2020-0-01389, Artificial Intelligence Convergence Research Center (Inha University)). Also, this research was supported by the National Research Foundation of Korea grant from the Korean Government (MSIT; the Ministry of Science and ICT) (grant no. NRF-2021M1A5A1075516) (KOPRI-PN21013).

References

Anderson, E.J., Mann, G.E., 2021. A high-amplitude atmospheric inertia–gravity wave-induced meteotsunami in Lake Michigan. Nat. Hazards 106, 1489–1501. https://doi.org/10.1007/s11069-020-04195-2.

Angove, M., Kozlosky, L., Chu, P., Dusek, G., Mann, G., Anderson, E., Gridley, J., Arcas, D., Titov, V., Eble, M., McMahon, K., Hirsch, B., Zaleski, W., 2021. Addressing the meteotsunami risk in the United States. Nat. Hazards 106, 1467–1487. https://doi.org/10.1007/s11069-020-04499-3.

Bechle, A.J., Wu, C.H., 2014. The Lake Michigan meteotsunamis of 1954 revisited. Nat. Hazards 74, 155–177. https://doi.org/10.1007/s11069-014-1193-5.

Choi, B.J., Hwang, C., Lee, S.H., 2014. Meteotsunami-tide interactions and high-frequency sea level oscillations in the eastern Yellow Sea. J. Geophys. Res. Ocean. 119, 6725–6742. https://doi.org/10.1002/2013JC009788.

Denamiel, C., Huan, X., Šepić, J., Vilibić, I., 2020. Uncertainty propagation using polynomial chaos expansions for extreme sea level hazard assessment: the case of the eastern Adriatic meteotsunamis. J. Phys. Oceanogr. 50, 1005–1021. https://doi.org/10.1175/JPO-D-19-0147.1.

Denamiel, C., Šepić, J., Ivanković, D., Vilibić, I., 2019. The Adriatic Sea and Coast modelling suite: Evaluation of the meteotsunami forecast component. Ocean Model. 135, 71–93. https://doi.org/10.1016/j.ocemod.2019.02.003.

Domps, B., Marmain, J., Guerin, C.A., 2021. A reanalysis of the October 2016 "Meteotsunami" in British Columbia with help of high-frequency radars and autoregressive modeling. IEEE.Geosci. Rem. Sens. Lett 19, 1–5. https://doi.org/10.1109/LGRS.2021.3066849.

Ferrarin, C., Bajo, M., Benetazzo, A., Cavaleri, L., Chiggiato, J., Davison, S., Davolio, S., Lionello, P., Orlić, M., Umgiesser, G., 2021. Local and large-scale controls of the exceptional Venice floods of November 2019. Prog. Oceanogr. 197, 102628 https://doi.org/10.1016/j.pocean.2021.102628.

Ha, T., Yoon, J.S., Heo, K.Y., 2018. Numerical simulations of a meteotsunami using both atmospheric and phase-resolving wave models in the Yellow Sea. J. Coast Res. 85, 786–790. https://doi.org/10.2112/SI85-158.1.

Horvath, K., Šepić, J., Prtenjak, M.T., 2018. Atmospheric forcing conducive for the Adriatic 25 June 2014 meteotsunami event. Pure Appl. Geophys. 175, 3817–3837. https://doi.org/10.1007/s00024-018-1902-1.

Huang, C., Anderson, E., Liu, Y., Ma, G., Mann, G., Xue, P., 2021. Evaluating essential processes and forecast requirements for meteotsunami-induced coastal flooding. Nat. Hazards 110, 1693–1718. https://doi.org/10.1007/s11069-021-05007-x.

Jansà, A., Ramis, C., 2021. The Balearic rissaga: from pioneering research to present-day knowledge. Nat. Hazards 106, 1269–1297. https://doi.org/10.1007/s11069-020-04221-3.

Kazeminezhad, M.H., Vilibić, I., Denamiel, C., Ghafarian, P., Negah, S., 2021. Weather radar and ancillary observations of the convective system causing the northern Persian Gulf meteotsunami on 19 March 2017. Nat. Hazards 106, 1747–1769. https://doi.org/10.1007/s11069-020-04208-0.

Kim, J., Omira, R., 2021. The 6–7 July 2010 meteotsunami along the coast of Portugal: insights from data analysis and numerical modelling. Nat. Hazards 106, 1397–1419. https://doi.org/10.1007/s11069-020-04335-8.

Kim, M.S., Eom, H., You, S.H., Woo, S.B., 2021a. Real-time pressure disturbance monitoring system in the Yellow Sea: pilot test during the period of March to April 2018. Nat. Hazards 106, 1703–1728. https://doi.org/10.1007/s11069-020-04245-9.

Kim, M.S., Woo, S.B., Eom, H., You, S.H., 2021b. Occurrence of pressure-forced meteotsunami events in the eastern Yellow Sea during 2010–2019. Nat. Hazards Earth Syst. Sci. 21, 3323–3337. https://doi.org/10.5194/nhess-21-3323-2021.

Kim, M.S., Woo, S.B., Eom, H., You, S.H., 2022. Progress report on addressing meteotsunami risk in the eastern Yellow Sea. Environ. Res. Lett. 17, 014009 https://doi.org/10.1088/1748-9326/ac3e21.

Kwon, K.M., Choi, B.J., Myoung, S.G., Sim, H.S., 2021. Propagation of a meteotsunami from the Yellow Sea to the Korea strait in April 2019. Atmosphere (Basel) 12, 1083. https://doi.org/10.3390/atmos12081083.

Ličer, M., Mourre, B., Troupin, C., Krietemeyer, A., Jansà, A., Tintoré, J., 2017. Numerical study of Balearic meteotsunami generation and propagation under synthetic gravity wave forcing. Ocean Model. 111, 38–45. https://doi.org/10.1016/j.ocemod.2017.02.001.

Linares, Á., Bechle, A.J., Wu, C.H., 2016. Characterization and assessment of the meteotsunami hazard in northern Lake Michigan. J. Geophys. Res. Ocean. 121, 7141–7158. https://doi.org/10.1002/2016JC011979.

Liu, Y., Wu, C.H., 2022. Drowning incidents and conditions due to hidden flash rips in Lake Michigan. Sci. Total Environ. 121, 154314 https://doi.org/10.1016/j.scitotenv.2022.154314.

Monserrat, S., Vilibić, I., Rabinovich, A.B., 2006. Meteotsunamis: atmospherically induced destructive ocean waves in the tsunami frequency band. Nat. Hazards Earth Syst. Sci. 6 https://doi.org/10.5194/nhess-6-1035-2006.

Mourre, B., Santana, A., Builes, A., Gautreau, L., Ličer, M., Jansà, A., Casas, B., Amengual B., Tintoré J., (2021). On the potential of ensemble forecasting for the prediction of meteotsunamis in the Balearic Islands: sensitivity to atmospheric model parameterizations. Nat. Hazards 106, 1315–1336. https://doi.org/10.1007/s11069-020-03908-x.

Pattiaratchi, C.B., Wijeratne, E.M.S., 2015. Are meteotsunamis an underrated hazard? Philos. Trans. R. Soc. A Math. Phys. Eng. Sci. https://doi.org/10.1098/rsta.2014.0377.

Perez, I., Dragani, W., 2021. Numerical study of meteotsunamis driven by atmospheric gravity waves in coastal waters of Buenos Aires Province, Argentina. Nat. Hazards 106, 1035–1051. https://doi.org/10.1007/s11069-020-04485-9.

Proudman, J., 1929. The effects on the sea of changes in atmospheric pressure. Geophys. Suppl. Mon. Notices R. Astron. Soc. 2, 197–209. https://doi.org/10.1111/j.1365-246X.1929.tb05408.x.

Rabinovich, A.B., 2009. Seiches and harbor oscillations. In: Handbook of Coastal and Ocean Engineering. World Sci., pp. 193–236. https://doi.org/10.1142/9789812819307_0009.

Rabinovich, A.B., 2020. Twenty-seven years of progress in the science of meteorological tsunamis following the 1992 Daytona Beach event. Pure Appl. Geophys. 177, 1193–1230. https://doi.org/10.1007/s00024-019-02349-3.

Rabinovich, A.B., Šepić, J., Thomson, R.E., 2021. The meteorological tsunami of 1 November 2010 in the southern Strait of Georgia: a case study. Nat. Hazards 106, 1503–1544. https://doi.org/10.1007/s11069-020-04203-5.

Romero, R., Vich, M., Ramis, C., 2019. A pragmatic approach for the numerical prediction of meteotsunamis in Ciutadella harbour (Balearic Islands). Ocean Model. 142, 101441 https://doi.org/10.1016/j.ocemod.2019.101441.

Šepić, J., Vilibić, I., 2011. The development and implementation of a real-time meteotsunami warning network for the Adriatic Sea. Nat. Hazards Earth Syst. Sci. 11, 83–91. https://doi.org/10.5194/nhess-11-83-2011.

Šepić, J., Denis, L., Vilibić, I., 2009. Real-time procedure for detection of a meteotsunami within an early tsunami warning system. Phys. Chem. Earth 34, 1023–1031. https://doi.org/10.1016/j.pce.2009.08.006.

Šepić, J., Vilibić, I., Fine, I., 2015a. Northern Adriatic meteorological tsunamis: assessment of their potential through ocean modeling experiments. J. Geophys. Res. Ocean. 120, 2993–3010. https://doi.org/10.1002/2015JC010795.

Šepić, J., Vilibić, I., Monserrat, S., 2016. Quantifying the probability of meteotsunami occurrence from synoptic atmospheric patterns. Geophys. Res. Lett. 43, 10377–10384. https://doi.org/10.1002/2016GL070754.

Šepić, J., Vilibić, I., Rabinovich, A.B., Monserrat, S., 2015b. Widespread tsunami-like waves of 23-27 June in the Mediterranean and Black Seas generated by high-Altitude atmospheric forcing. Sci. Rep. 5, 11682 https://doi.org/10.1038/srep11682.

Shi, L., Olabarrieta, M., Valle-Levinson, A., Warner, J.C., 2019. Relevance of wind stress and wave-dependent ocean surface roughness on the generation of winter meteotsunamis in the Northern Gulf of Mexico. Ocean Model. 140, 101408 https://doi.org/10.1016/j.ocemod.2019.101408.

Titov, V., Moore, C., 2021. Meteotsunami model forecast: can coastal hazard be quantified in real time? Nat. Hazards 106, 1545–1561. https://doi.org/10.1007/s11069-020-04450-6.

Tojčić, I., Denamiel, C., Vilibić, I., 2021. Performance of the Adriatic early warning system during the multi-meteotsunami event of 11-19 May 2020: an assessment using energy banners. Nat. Hazards Earth Syst. Sci. 21, 2427–2446. https://doi.org/10.5194/nhess-21-2427-2021.

Vilibić, I., 2008. Numerical simulations of the Proudman resonance. Continent. Shelf Res. 28, 574–581. https://doi.org/10.1016/j.csr.2007.11.005.

Vilibić, I., Rabinovich, A.B., Anderson, E.J., 2021. Special issue on the global perspective on meteotsunami science: editorial. Nat. Hazards 106, 1087–1104. https://doi.org/10.1007/s11069-021-04679-9.

Vilibić, I., Šepić, J., Dunić, N., Sevault, F., Monserrat, S., Jordà, G., 2018. Proxy-based assessment of strength and frequency of meteotsunamis in future climate. Geophys. Res. Lett. 45, 10501–10508. https://doi.org/10.1029/2018GL079566.

Vilibić, I., Šepić, J., Rabinovich, A.B., Monserrat, S., 2016. Modern approaches in meteotsunami research and early warning. Front. Mar. Sci. 3, 1–7. https://doi.org/10.3389/fmars.2016.00057.

Wang, J.W., Yang, H.J., Kim, J.J., 2020. Wind speed estimation in urban areas based on the relationships between background wind speeds and morphological parameters. J. Wind Eng. Ind. Aerod. 205, 104324 https://doi.org/10.1016/j.jweia.2020.104324.

Wang, Y., Niu, X., Yu, Z., Gao, X., 2021. Numerical study on a possible cause of the 'strange tide' in the coastal area of Jiangsu Province, China. Nat. Hazards 106, 1687–1701. https://doi.org/10.1007/s11069-020-04111-8.

Wertman, C.A., Yablonsky, R.M., Shen, Y., Merrill, J., Kincaid, C.R., Pockalny, R.A., 2014. Mesoscale convective system surface pressure anomalies responsible for meteotsunamis along the U.S. East Coast on June 13th, 2013. Sci. Rep. 4, 7143. https://doi.org/10.1038/srep07143.